

This manuscript has been authored by UT-Battelle, LLC under Contract No. DE-AC05-00OR22725 with the U.S. Department of Energy. The United States Government retains and the publisher, by accepting the article for publication, acknowledges that the United States Government retains a non-exclusive, paid-up, irrevocable, world-wide license to publish or reproduce the published form of this manuscript, or allow others to do so, for United States Government purposes. The Department of Energy will provide public access to these results of federally sponsored research in accordance with the DOE Public Access Plan (<http://energy.gov/downloads/doe-public-access-plan>).

Strengthening the magnetic interactions in pseudobinary first-row transition metal thiocyanates, $M(\text{NCS})_2$

Euan N. Bassey,¹ Joseph A. M. Paddison,^{2,3,4} Evan N. Keyzer,¹ Jeongjae Lee,^{1,5} Pascal Manuel,⁶ Ivan da Silva,⁶ Siân E. Dutton,³ Clare P. Grey^{1,*} and Matthew J. Cliffe^{1,7,*}

¹Department of Chemistry, Lensfield Road, University of Cambridge, CB2 1EW, United Kingdom

²Churchill College, University of Cambridge, Storey's Way, Cambridge, CB3 0DS, United Kingdom

³Cavendish Laboratory, Department of Physics, University of Cambridge, JJ Thompson Avenue, Cambridge, CB3 0HE, United Kingdom

⁴Materials Science & Technology Division, Oak Ridge National Laboratory, Oak Ridge, TN 37831, United States of America

⁵School of Earth and Environmental Sciences, Seoul National University, Seoul 08826, Korea

⁶ISIS Facility, STFC Rutherford Appleton Laboratory, Harwell Oxford, Didcot, OX11 0QX, United Kingdom

⁷School of Chemistry, University Park, Nottingham, NG7 2RD, United Kingdom

ABSTRACT: Understanding the effect of chemical composition on the strength of magnetic interactions is key to the design of magnets with high operating temperatures. The magnetic divalent first-row transition metal (TM) thiocyanates are a class of chemically simple layered molecular frameworks. Here, we report two new members of the family, manganese (II) thiocyanate, $\text{Mn}(\text{NCS})_2$, and iron (II) thiocyanate, $\text{Fe}(\text{NCS})_2$. Using magnetic susceptibility measurements on these materials and on cobalt (II) thiocyanate and nickel (II) thiocyanate, $\text{Co}(\text{NCS})_2$ and $\text{Ni}(\text{NCS})_2$, respectively, we identify significantly stronger net antiferromagnetic interactions between the earlier TM ions—a decrease in the Weiss constant, θ , from 29 K for $\text{Ni}(\text{NCS})_2$ to -115 K for $\text{Mn}(\text{NCS})_2$ —a consequence of more diffuse $3d$ orbitals, increased orbital overlap and increasing numbers of unpaired t_{2g} electrons. We elucidate the magnetic structures of these materials: $\text{Mn}(\text{NCS})_2$, $\text{Fe}(\text{NCS})_2$ and $\text{Co}(\text{NCS})_2$ order into the same antiferromagnetic commensurate ground state, whilst $\text{Ni}(\text{NCS})_2$ adopts a ground state structure consisting of ferromagnetically ordered layers stacked antiferromagnetically. We show that magnetic molecular frameworks with significantly stronger net exchange interactions can be constructed by using earlier TMs.

1. INTRODUCTION

The rational design and synthesis of new magnetic materials tailored to particular functions requires an understanding of the fundamental interactions taking place between magnetic centres. Magnetic molecular framework materials—that is, systems in which magnetic centres are connected *via* molecular ligands into lattices—present an excellent opportunity to study these interactions and their chemical origins.

Using molecular bridging ligands to connect paramagnetic metal centres can produce open and flexible structures, permitting potential applications such as multiferroics,^{1–3} magnetostrictive materials⁴ and magnetic sensors.^{5–7} The properties of molecular frameworks are not determined by long-range electrostatic forces—as in oxide frameworks—but are instead dominated by short-range covalent bonds between the metal centre, M and its ligands, L .⁸ The nature and delocalisation of the $M-L$ bond controls the exchange interactions and therefore the magnetic properties of the material. By careful choice of L , very anisotropic structures can be

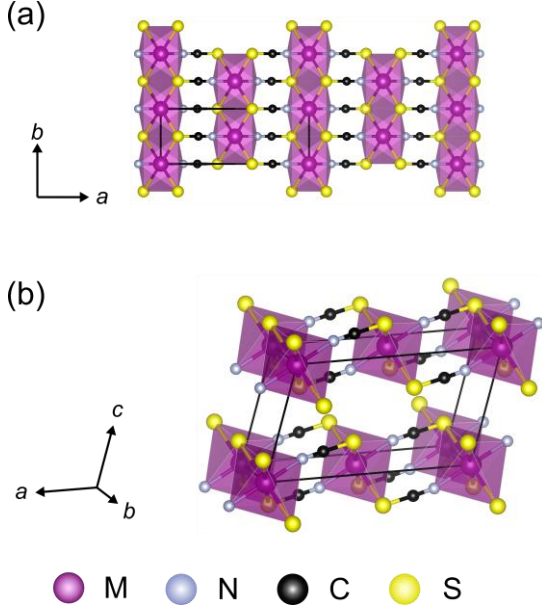


Figure 1. (a) Projection of a (2x2x1) supercell of $M(\text{NCS})_2$ ($M = \text{Mn, Fe, Co, Ni}$) down the c axis, highlighting the layers of edge- and corner-sharing M^{2+} octahedra. (b) The monoclinic unit cell (space group $C2/m$), as reported in Refs. 19 and 26.

created, which may have low-dimensional magnetic properties.^{9–14}

Low dimensional magnetic materials are an example of many-body quantum systems amenable to exact mathematical treatment.¹⁵ In particular, the study of the behaviour of low-dimensional magnets is of critical importance to spin-liquids^{16,17} and high-temperature superconductivity.¹⁸

Thiocyanate, $(\text{NCS})^-$, is a promising ligand in magnetic molecular frameworks, as it is capable of promoting strong superexchange interactions between paramagnetic metal centres—for example, $J = +230$ K in $\text{Cu}_2(\text{NCS})_4(\text{bpm})$ ($\text{bpm} = 2,2\text{-bipyrimidine}$).^{9,19–24} However, the majority of the frameworks studied thus far incorporate ancillary ligands, which can decrease metal-metal connectivity in the framework and thereby the net strength of interactions (as measured by the Weiss constant, θ).^{19,20}

Despite the range of complex magnetic thiocyanate compounds reported,²⁵ the parent pseudobinary system, $M(\text{NCS})_2$, is relatively unexplored, with only three known magnetic examples: $\text{Co}(\text{NCS})_2$,¹⁹ $\text{Ni}(\text{NCS})_2$,^{26,27} and $\text{Cu}(\text{NCS})_2$.⁹ $\text{Cu}(\text{NCS})_2$ is a quasi-one-dimensional magnet, due to the Jahn-Teller distortion of the Cu^{2+} ions, with strong superexchange interactions along the

$\text{Cu}(\text{NCS})_2$ chain ($J = 133$ K), but a significantly lower Néel temperature, $T_N = 12$ K.⁹

Previous work has established that both $\text{Co}(\text{NCS})_2$ ¹⁹ and $\text{Ni}(\text{NCS})_2$ ²⁷ order antiferromagnetically, with $T_N = 22$ K and 52 K, respectively. However, the value of θ for $\text{Ni}(\text{NCS})_2$ suggested net ferromagnetic interactions ($\theta = 39.8$ K);²⁷ in contrast, $\text{Co}(\text{NCS})_2$ has net antiferromagnetic interactions ($\theta = -40$ K).¹⁹ At present, the magnetic structures of $\text{Co}(\text{NCS})_2$ and $\text{Ni}(\text{NCS})_2$ are unknown, which makes rationalising the differences in the values of θ challenging.

The structures adopted by $M(\text{NCS})_2$ are directly analogous to the corresponding transition metal (TM) halides, MX_2 [Figure 1]. MX_2 consist of layers of edge-sharing M^{2+} octahedra with weak van der Waals interactions between the layers [Figure 1].^{19,26} The triangular metal sublattice lends itself to geometric frustration,²⁸ and hence leads to unusual magnetic properties, such as multiferroic behaviour and helimagnetism.^{29–33}

In $M(\text{NCS})_2$ ($M = \text{Co, Ni}$), the metal sites form layers of an anisotropic triangular lattice, and so $M(\text{NCS})_2$ have the potential to show similar unusual magnetic behaviour. The two nearest-neighbour interactions within the layers are J_1 , along the $M\text{--}S\text{--}M$ chains (along the $[010]$ direction), and J_2 , through $M\text{--}NCS\text{--}M$ linkages [Figure 2(b) and (c)]; the Heisenberg Hamiltonian for this system may be written as:

$$\hat{H} = \sum_{i,j} S_i J_{ij} S_j, \quad (1)$$

where the summation is taken over all nearest-neighbour pairs of spins i and j with a Heisenberg exchange constant J_{ij} between them. Here, each pair is counted once and positive values of J_{ij} correspond to antiferromagnetic interactions.

The spatially anisotropic triangular lattice may be characterised using a single parameter, $\phi = \tan^{-1} \left(\frac{J_1}{J_2} \right)$ [Figure 2(a)].^{34,35} By varying J_1 and J_2 , the isotropic triangular lattice ($J_1 = J_2$, $\phi = \frac{\pi}{4}$) can be transformed into a square lattice ($J_1 = 0$, $\phi = 0, \pi$), or a quasi-one-dimensional chain ($J_2 = 0$, $\phi = \frac{\pi}{2}$). Although we anticipate that the presence of a small finite interlayer coupling (J_3 , where we expect $J_3 \ll J_1, J_2$), this two-dimensional phase diagram will still provide a qualitative reference for the observed phases,

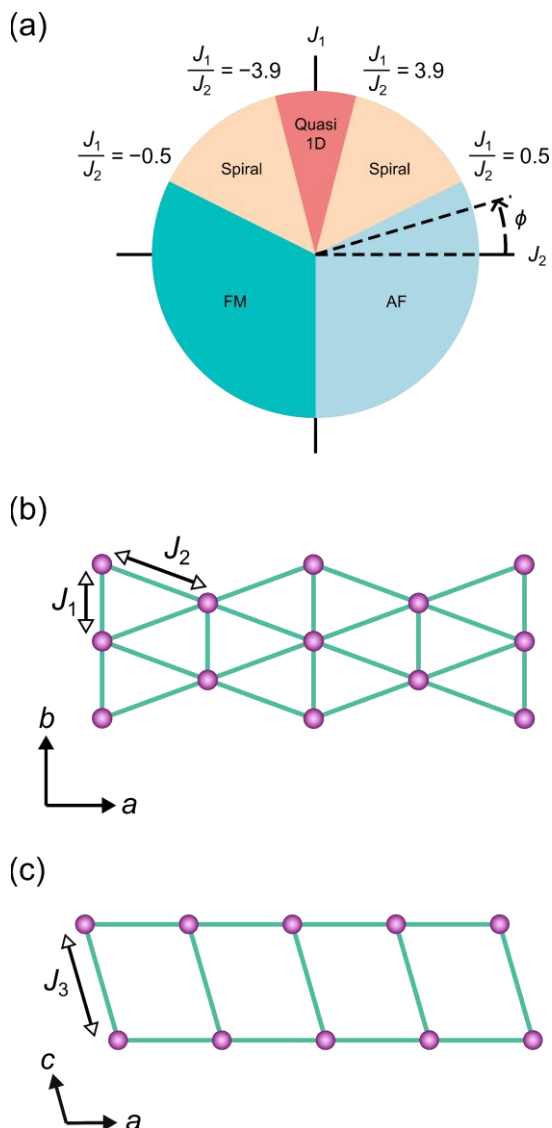


Figure 2. (a) Classical Heisenberg magnetic phase diagram for an anisotropic two-dimensional triangular lattice, with exchange interactions J_1 and J_2 , as illustrated in **(b)**. The interlayer coupling constant, J_3 , for the $M(\text{NCS})_2$ lattice is illustrated in **(c)**. Figure adapted from Ref. 35.

as has been found for other van der Waals magnets.^{29–32,36}

In this work, we synthesised and characterised $M(\text{NCS})_2$ ($M = \text{Mn}, \text{Fe}, \text{Co}$ and Ni)— $M = \text{Mn}$ and Fe for the first time. The materials were characterised using powder X-ray diffraction, thermogravimetric analysis and diffuse reflectance spectroscopy. In addition, we measured their magnetic properties using magnetic susceptibility measurements and powder neutron diffraction (PND) and determined constraints on the relative sizes of their magnetic exchange interactions.

We show that the net strength of superexchange interactions, as measured by the Weiss constant, θ , increases and becomes increasingly antiferromagnetic as we move to earlier first-row TM cations.

From PND measurements, $\text{Mn}(\text{NCS})_2$, $\text{Fe}(\text{NCS})_2$ and $\text{Co}(\text{NCS})_2$ are observed to adopt the same commensurate stripe-ordered magnetic ground state with ordering vector $\mathbf{k} = [100]^*$. In contrast, $\text{Ni}(\text{NCS})_2$ adopts a ground state magnetic structure with ordering vector $\mathbf{k} = [00 \frac{1}{2}]^*$, consistent with its very different (and positive) Weiss constant.

2. MATERIALS AND METHODS

2.1. Synthesis

2.1.1. $\text{Mn}(\text{NCS})_2$ $\text{MnSO}_4 \cdot \text{H}_2\text{O}$ (Sigma Aldrich, 99%, 1.690 g, 10.00 mmol) was dissolved in the minimum volume of deionised H_2O to yield a pale pink solution. A saturated solution of $\text{Ba}(\text{SCN})_2 \cdot 3\text{H}_2\text{O}$ (Alfa Aesar, 98%, 3.075 g, 10.00 mmol) was added to this in portions, forming a white precipitate immediately. The reaction mixture was stirred overnight and the precipitate isolated by centrifugation and then decanting the supernatant liquor. The solvent was removed *in vacuo* to yield a yellow residue, which was dried by heating in air at 120°C for one hour before further drying under dynamic vacuum for 48 hours at 100°C . Manganese (II) thiocyanate (1.460 g, 6.01 mmol, 60%) was collected as a pale yellow microcrystalline powder. The same procedure—with all quantities scaled up by a factor of 6.5—was used to synthesise the sample used for neutron diffraction measurements. This compound readily hydrates in ambient humidity, turning from pale yellow to green; as such, it was stored in a dry argon atmosphere.

The product was analysed for elemental purity (combustion analysis for CHN). Found (calculated) $\text{C}_2\text{N}_2\text{S}_2\text{Mn}$: C 13.32% (14.04%), H 0.05% (0.00%), N 15.32% (16.37%).

2.1.2. $\text{Fe}(\text{NCS})_2$ KSCN (Sigma Aldrich, 99%, 0.117 g, 1.2 mmol) was dissolved in dry acetonitrile (approximately 20 cm^3) and the clear colourless solution stirred under a nitrogen atmosphere at room temperature. The solution was added to $\text{Fe}(\text{BF}_4)_2 \cdot 6\text{H}_2\text{O}$ (Aldrich, 97%, 0.203 g, 0.6 mmol), instantly forming a

dark red solution. The reaction mixture was stirred under a nitrogen atmosphere at room temperature for approximately five minutes, separating to a dark red solution and white precipitate (coloured red by the strongly-coloured supernatant liquor). The mixture was filtered *via* a cannula and the supernatant liquor taken to dryness *in vacuo* to yield a dark red-purple residue, which was heated under dynamic vacuum to form an orange-brown powder. Iron(II) thiocyanate (0.047 g, 0.27 mmol, 45%) was isolated as an orange-brown microcrystalline powder. The same procedure—with all reagent masses scaled up by a factor of 33—was used to synthesise the sample used for neutron diffraction measurements. The compound is air sensitive, oxidising to form a dark brown powder; as such, the compound was stored under inert atmosphere.

The product was analysed for elemental purity (combustion analysis for CHN). Found (calculated) $C_2N_2S_2Fe$: C 13.60% (13.97%), H 0.10% (0.00%), N 15.39% (16.29%).

2.1.3. $Co(NCS)_2$ $CoSO_4 \cdot 7H_2O$ (Sigma Aldrich, 99%, 2.811 g, 10.00 mmol) was dissolved in the minimum volume of deionised H_2O to generate a clear red solution. A saturated solution of $Ba(SCN)_2 \cdot 3H_2O$ (Alfa Aesar, 98%, 3.075 g, 10.00 mmol) in deionised H_2O was added in portions, instantly forming a white precipitate, coloured by the strong red supernatant liquor. The reaction mixture was left to stir at room temperature overnight, and the precipitate isolated by centrifugation and then decanting the supernatant liquor. The supernatant liquor was dried *in vacuo*, generating a red-brown residue, which was further dried by heating in air at approximately 120°C for one hour. Cobalt (II) thiocyanate (1.257 g, 7.18 mmol, 72%) was collected as a red-brown microcrystalline powder. The same procedure—with all quantities scaled up by a factor of 6.5—was used to synthesise the sample used for neutron diffraction measurements.

2.1.4. $Ni(NCS)_2$ $NiSO_4 \cdot 6H_2O$ (Alfa Aesar, 99.97%, 2.628 g, 10.00 mmol) was dissolved in the minimum volume of deionised H_2O , forming a clear green solution. To this, a saturated solution of $Ba(SCN)_2 \cdot 3H_2O$ (Alfa Aesar, 98%, 3.075 g, 10.00 mmol) in deionised H_2O was added, instantly forming a white precipitate, coloured green by the supernatant liquor. The reaction mixture was stirred at room

temperature overnight and the precipitate removed with a centrifuge. The liquor was dried *in vacuo* to generate a green-brown microcrystalline powder. Nickel (II) thiocyanate (1.501 g, 8.58 mmol, 86%) was collected as a green-brown microcrystalline powder. The same procedure—with all quantities scaled up by a factor of 6.5—was used to synthesise the sample used for neutron diffraction measurements.

2.2. Powder X-Ray Diffraction (PXRD) Phase purity was assessed *via* powder diffraction measurements on a PANalytical Empyrean Diffractometer using Cu-K α radiation ($\lambda = 1.541 \text{ \AA}$) in Bragg-Brentano geometry. Diffraction patterns were recorded over the range $2\theta = 5\text{--}80^\circ$ using a step size of 0.02° and a scan speed of $0.01^\circ \text{ s}^{-1}$. Due to their sensitivity to moisture and air, the diffraction patterns of $Mn(NCS)_2$ and $Fe(NCS)_2$ were measured by encasing the samples between polyimide (Kapton) films. All diffraction patterns were analysed *via* Pawley³⁷ and Rietveld^{38,39} refinements using TOPAS Academic 6 structure refinement software.^{40,41}

2.3. Diffuse Reflectance Spectroscopy Diffuse reflectance spectra were recorded on an Agilent Technologies UV-VIS spectrometer, connected *via* optical fibre to a Cary 50 Diffuse Reflectance Accessory, using a wavelength range $\lambda = 200 - 1000 \text{ nm}$, with step size 1.00 nm and scan rate of 10 nm s^{-1} . Samples of $Mn(NCS)_2$ and $Fe(NCS)_2$ were mounted onto the quartz discs inside an argon-filled glovebox and quickly transported to the spectrometer (within half an hour) for analysis. $Mn(NCS)_2$ was diluted with $BaSO_4$ powder in a 1:1 mass ratio and the mixture ground together to produce a homogeneous powder; $Fe(NCS)_2$, $Co(NCS)_2$ and $Ni(NCS)_2$ were mixed in 1:10 ($M(NCS)_2$: $BaSO_4$) mass ratios and the mixture ground together to produce homogeneous powders. Samples were loaded between two quartz discs and sealed with Parafilm. The spectra were averaged over multiple measurements; spikes in the average due to erroneous spikes in the raw data—i.e. spikes in one spectrum which do not repeat in the other spectra, likely due to specular reflection from the powder—were removed from the average and the ‘spiked’ data point replaced with the average intensity either side of the spike.

2.4. Thermogravimetric Analysis (TGA) Thermogravimetric data for each compound were recorded with a Mettler-Toledo

Thermogravimetric Analysis/Simultaneous Differential Thermal Analysis (TGA/SDTA) 851 Thermobalance. Each powder sample (20 – 50 mg) was loaded into an alumina crucible and heated from 50°C to 600°C at a heating rate of 10°C min⁻¹ under a nitrogen atmosphere. The data collected was measured relative to a background blank TGA curve, recorded using the same alumina crucible, temperature range and heating rate, under a nitrogen atmosphere.

2.5. Magnetic Susceptibility Measurements

The magnetic susceptibility measurements were carried out on powder samples (10 – 20 mg) using a Quantum Design Magnetic Property Measurement System 3 (MPMS) superconducting quantum interference device (SQUID) magnetometer. The zero-field cooled (ZFC) and field-cooled (FC) susceptibilities were measured in a field of 0.01 T over a temperature range 2 – 300 K. As $M(H)$ is linear in this field range, the small-field approximation to the susceptibility, $\chi \simeq \frac{M}{H}$, was assumed to be valid. The data for each compound were corrected for diamagnetism of the sample using Pascal's constants.⁴²

2.6. Powder Neutron Diffraction (PND)

Powder neutron diffraction measurements were carried out at the ISIS Pulsed Neutron and Muon Source using the WISH (Mn(NCS)₂, Co(NCS)₂, Ni(NCS)₂) and GEM (Fe(NCS)₂) instruments.⁴³ Samples of Mn(NCS)₂ (4.76 g), Fe(NCS)₂ (2.26 g), Co(NCS)₂ (2.44 g) and Ni(NCS)₂ (4.76 g) were loaded into thin-walled vanadium canisters. The canister diameters were 11 mm for Mn(NCS)₂ and Ni(NCS)₂; 6 mm for Co(NCS)₂ and 6 mm with an indium seal for Fe(NCS)₂. Each sample was loaded to a height of at least 40 mm, to ensure the full beam illuminates the sample.

Each sample was first cooled to the base temperature (1.5 K for Mn(NCS)₂, Co(NCS)₂ and Ni(NCS)₂ and 10 K for Fe(NCS)₂) and diffraction patterns then collected at a series of temperatures through T_N . The complete list of temperature steps and data collections may be found in the supporting information. The data were corrected for absorption effects using the Mantid software package.⁴⁴

For each structure, the nuclear structure was determined by Rietveld refinement against powder neutron diffraction data collected above T_N , using a model derived from the previously reported single crystal structure of Ni(NCS)₂.²⁶

All refinements were carried out using TOPAS Academic 6.0.⁴¹

Rietveld refinements using the candidate magnetic irreducible representations (irreps) were carried out for each compound separately, which showed that in each case only one of the two single irrep structures was consistent with the experimental data. Including the second irrep did not significantly improve the fit to the data. On this basis, we refined the magnetic structures using only the mY_2^+ irrep for Mn(NCS)₂, Co(NCS)₂ and Fe(NCS)₂, and the mA_1^+ irrep for Ni(NCS)₂. All refinements were carried out by simultaneously refining against data collected on multiple banks of detectors: on WISH, for Mn(NCS)₂, banks 2 – 5; for Co(NCS)₂, banks 1 – 5 and for Ni(NCS)₂, banks 2 – 5; on GEM, for Fe(NCS)₂, banks 2 – 5.

For the final refinements of the data collected for Mn(NCS)₂ using the WISH diffractometer and for the final refinement of the data collected for Fe(NCS)₂ on the GEM diffractometer, it proved necessary to refine the Voigt peak-shape parameters separately for high Q and low Q data, due to their unusual Q-dependence.

For all refinements, the lattice parameters, atomic positions and the magnitudes and directions of the magnetic moments were allowed to refine freely, aside from restraints on the C–N (ca. 1.15 Å) and C–S (ca. 1.65 Å) bond lengths. In all cases, the same set of freely refining anisotropic atomic displacement parameters was used for each atom [Table S6] and the bond lengths and angles were consistent with those expected from previous studies [Table S1].^{19,26}

3. RESULTS

3.1. Bulk characterisation The $M(\text{NCS})_2$ family members ($M = \text{Mn}^{2+}$, Fe^{2+} , Co^{2+} , Ni^{2+}) were synthesised *via* salt metathesis reactions, driven by precipitation of an insoluble side-product (BaSO₄ for $M = \text{Mn}$, Co , Ni ; KBF₄ for $M = \text{Fe}$). Apart from Ni(NCS)₂, all compounds crystallised as solvates; the co-crystallised solvent was removed by heating either *in vacuo* ($M = \text{Fe}$, Mn) or in air ($M = \text{Co}$). The phase purity of all materials was checked initially using PXRD [Figure S1], revealing the presence of trace quantities (< 1 wt. %) of impurities such as unreacted starting materials or hydrates. To

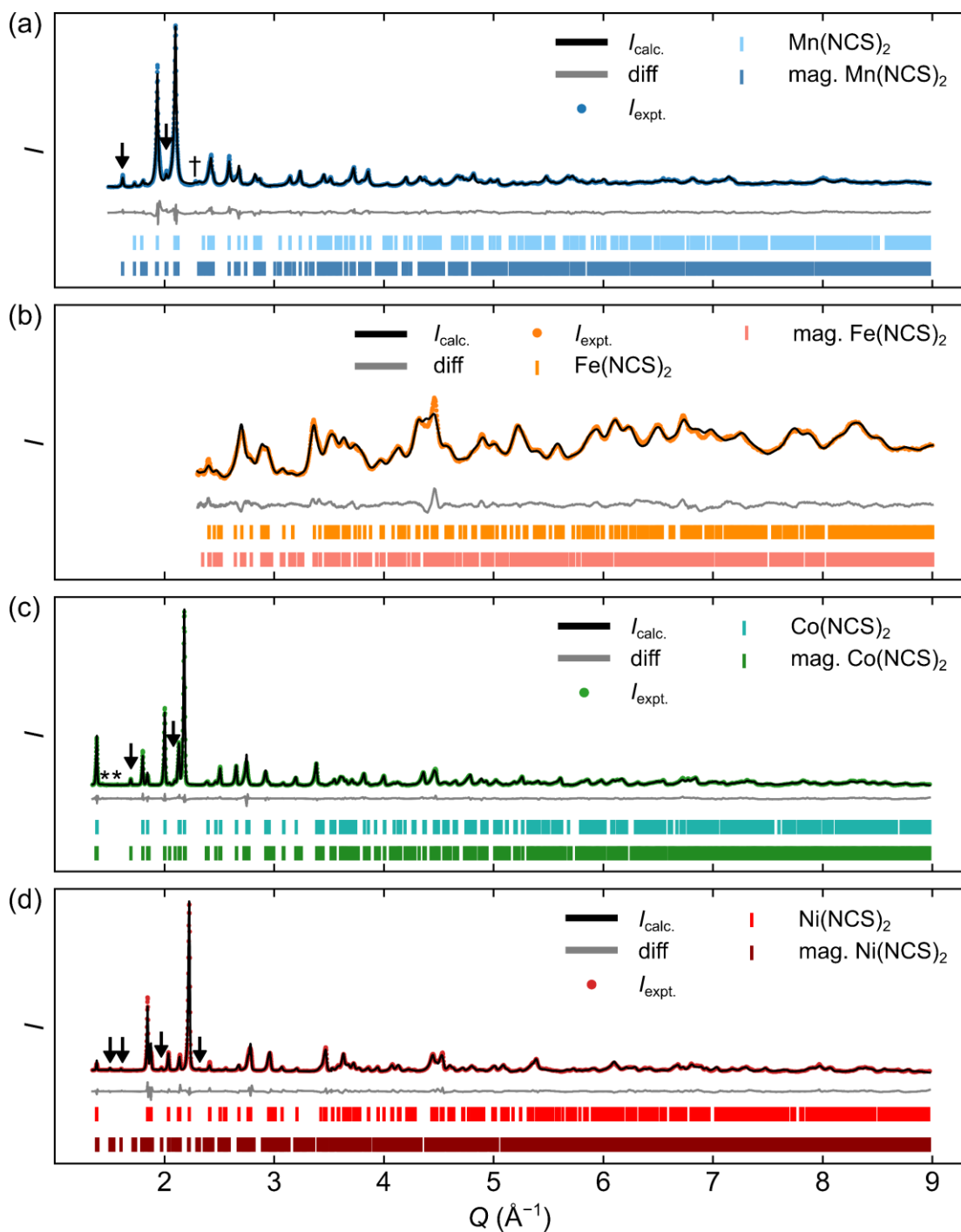


Figure 3. Rietveld refinements of the neutron powder diffraction patterns collected at 1.5 K for Mn(NCS)_2 , **(a)**; at 1.5 K for Co(NCS)_2 , **(c)** and 1.5 K for Ni(NCS)_2 **(d)**, all on Bank 5 of WISH. **(b)** shows the pattern collected at 10 K for Fe(NCS)_2 on Bank 5 of GEM. Arrows lie directly above magnetic peaks, asterisks are directly above magnetic reflections from impurity phases, whilst daggers are directly above non-magnetic reflections from impurity phases. $R_{\text{wp}} = 7.539\%$ for Mn(NCS)_2 , 3.303% for Fe(NCS)_2 , 4.061% for Co(NCS)_2 and 6.253% for Ni(NCS)_2 . The low- Q regions of the diffraction patterns are shown in more detail in Figure 8, to emphasize the magnetic Bragg peaks.

confirm whether any solvent remained trapped in the synthesised frameworks, we carried out thermogravimetric analysis (TGA) [Figure S2], which revealed minimal quantities of water lost from each material.

Quantitative Rietveld refinements of the high- Q powder neutron diffraction (PND) data collected confirmed that all four compounds were isostructural [Figure 3], crystallising in the space group $C2/m$, as anticipated for the similar

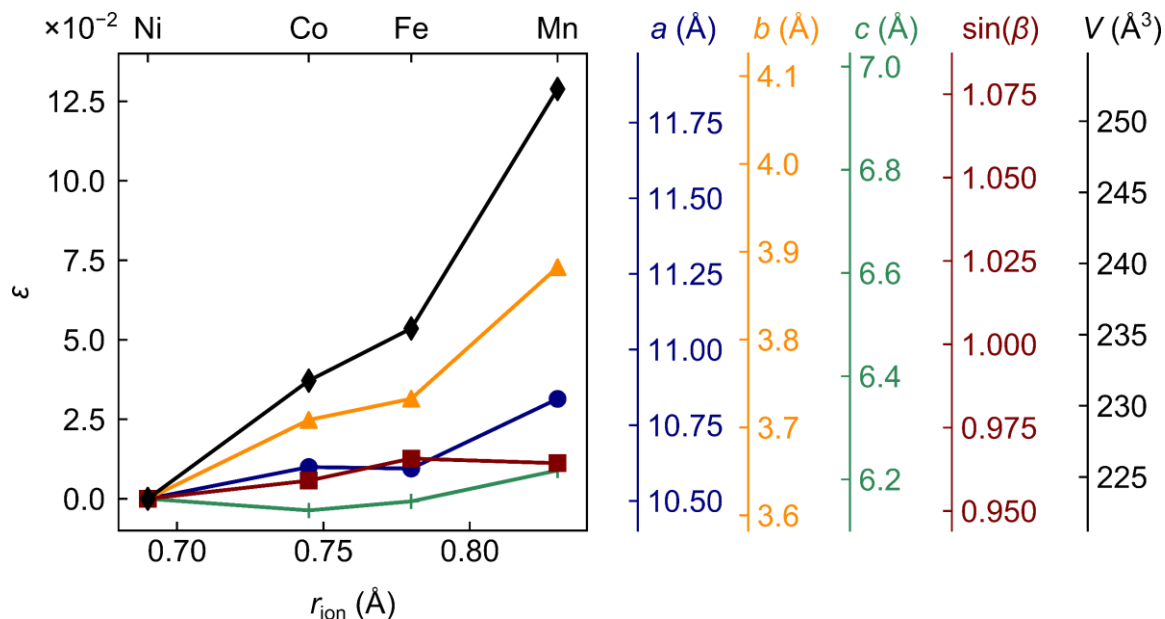


Figure 4. Variation in the strain of Rietveld-derived PND lattice parameters and nuclear unit cell volume (at the base temperature of PND results) with the ionic radius of M^{2+} , r_{ion} . The strain in each parameter, x ($x = a, b, c, \sin(\beta), V$), is calculated via $\varepsilon = \frac{x - x_{\text{Ni}}}{x_{\text{Ni}}}$ – i.e. the strain is calculated relative to the parameters obtained for $\text{Ni}(\text{NCS})_2$. The corresponding values of the lattice parameters are shown on the right-hand axes.

chemistries and ionic radii of the divalent first row TM cations.⁴⁵

The lattice parameters and atomic coordinates derived from Rietveld refinements are shown in Table 1. The lattice parameters and unit cell volume vary approximately linearly with cationic radius, r_{ion} [Figure 4]. The b lattice parameter depends only on the M – S bond lengths and M – S – M bond angle and therefore changes proportionately the most as M varies. The observed changes in b are also consistent with the expected differences in M – S bond lengths across the TM series.²⁰ The a lattice parameter is dominated by the length of $(\text{NCS})^-$ anion (which lies along the a axis), rather than the M – N and M – S bonds (which are oriented at an angle to the a direction) [Figure 1]. Since the length of $(\text{NCS})^-$ remains approximately constant regardless of the identity of M , changes in M have a small effect on the size of a . The c lattice parameter remains approximately constant across the series and is determined by the interlayer van der Waals interactions, suggesting these interactions have similar strengths across the first-row TM series.

All compounds except $\text{Mn}(\text{NCS})_2$ were strongly coloured microcrystalline powders: $\text{Fe}(\text{NCS})_2$ was orange-brown, $\text{Co}(\text{NCS})_2$ was red-brown¹⁹ and $\text{Ni}(\text{NCS})_2$ green-brown; $\text{Mn}(\text{NCS})_2$ was pale yellow.²⁶ To quantitatively assess the

variation in observed colours across the $M(\text{NCS})_2$ series, we recorded diffuse reflectance UV-Vis spectra [Figure 5(a)].

The observed intense transitions correspond to ligand-to-metal charge transfer (LMCT) transitions: from states dominated by $(\text{NCS})^-$ -based orbitals to states dominated by the metal $3d$ orbitals.^{46–48} The additional weak absorption bands observed for $\text{Fe}(\text{NCS})_2$, $\text{Co}(\text{NCS})_2$ and $\text{Ni}(\text{NCS})_2$ likely correspond to d – d transitions.⁴⁹ The optical (indirect) band gaps were extracted using Tauc fits to the data [Figure 5(b)],⁵⁰ giving the following values: 4.2(1) eV for $\text{Mn}(\text{NCS})_2$, 3.2(1) eV for $\text{Fe}(\text{NCS})_2$, 3.2(1) eV for $\text{Co}(\text{NCS})_2$ and 2.5(1) eV for $\text{Ni}(\text{NCS})_2$. On moving to later TM ions, the d orbitals decrease in energy and the crystal field splitting increases, resulting in a lower energy (longer wavelength) transition and smaller band gap. This trend is consistent with the small observed band gap for $\text{Cu}(\text{NCS})_2$ (1.3 eV), which is lowered further due to Jahn-Teller distortions of the Cu^{2+} ions.⁹

3.2. Bulk magnetic measurements To assess the change in the magnetic properties as the identity of M in $M(\text{NCS})_2$ varies, we next went on to measure the bulk magnetic susceptibilities of these compounds at $H = 0.01$ T [Figure 6].

Table 1. Rietveld-derived lattice parameters and atomic coordinates, based on the powder neutron diffraction data collected at 1.5 K for $\text{Mn}(\text{NCS})_2$, $\text{Co}(\text{NCS})_2$ and $\text{Ni}(\text{NCS})_2$ and at 10 K for $\text{Fe}(\text{NCS})_2$. The space group for all compounds is $C2/m$.

$\text{Mn}(\text{NCS})_2$					
	a (Å)	10.8370(17)	α (°)	90	
	b (Å)	3.8824(6)	β (°)	105.348(2)	
	c (Å)	6.2175(9)	γ (°)	90	
	Site	x	y	z	
Mn	2a	0	0	0	
N	4i	-0.1445(2)	0	0.1723(4)	
C	4i	-0.2465(4)	0	0.2278(6)	
S	4i	-0.3743(7)	0	0.2721(11)	
$\text{Fe}(\text{NCS})_2$					
	a (Å)	10.6068(13)	α (°)	90	
	b (Å)	3.7327(5)	β (°)	105.043(6)	
	c (Å)	6.1575(9)	γ (°)	90	
	Site	x	y	z	
Fe	2a	0	0	0	
N	4i	-0.14085(11)	0	0.17558(18)	
C	4i	-0.24005(12)	0	0.2215(3)	
S	4i	-0.3849(3)	0	0.2700(4)	
$\text{Co}(\text{NCS})_2$					
	a (Å)	10.6118(4)	α (°)	90	
	b (Å)	3.70869(11)	β (°)	106.4401(8)	
	c (Å)	6.13996(19)	γ (°)	90	
	Site	x	y	z	
Co	2a	0	0	0	
N	4i	-0.13799(7)	0	0.17056(13)	
C	4i	-0.23820(11)	0	0.2171(2)	
S	4i	-0.3782(2)	0	0.2610(4)	
$\text{Ni}(\text{NCS})_2$					
	a (Å)	10.5070(5)	α (°)	90	
	b (Å)	3.61889(5)	β (°)	107.509(3)	
	c (Å)	6.16252(16)	γ (°)	90	
	Site	x	y	z	
Ni	2a	0	0	0	
N	4i	-0.1325(2)	0	0.1699(4)	
C	4i	-0.2367(3)	0	0.2086(7)	
S	4i	-0.3778(6)	0	0.2543(9)	

All four compounds showed evidence of three-dimensional antiferromagnetic ordering [Figure 6]: a sharp change in $\frac{d\chi}{dT}$ at T_N and a rapid decrease in χ at low temperatures. Each compound also shows a rise in the

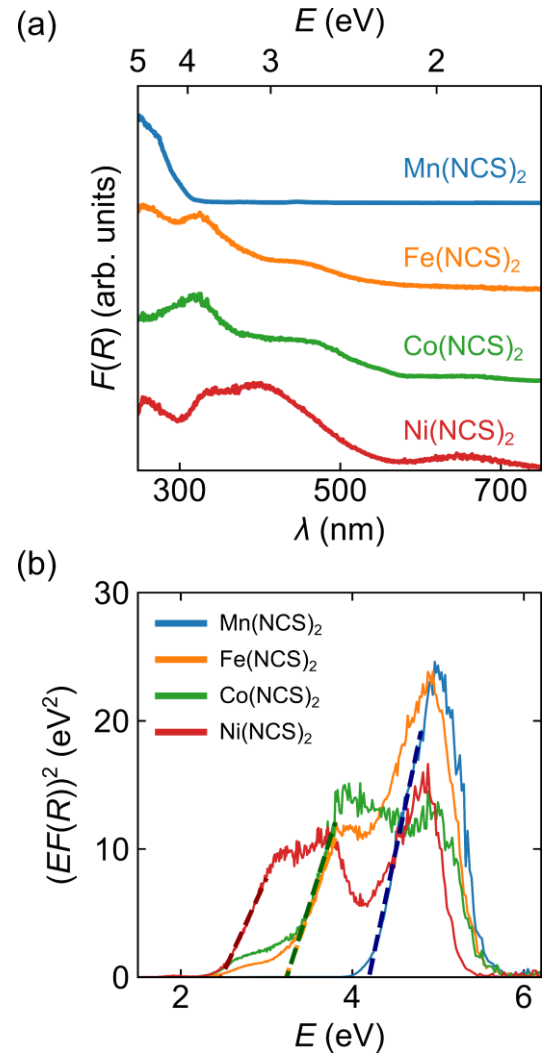


Figure 5. (a) Diffuse reflectance spectra for $M(\text{NCS})_2$ ($M = \text{Mn}, \text{Fe}, \text{Co}, \text{Ni}$). (b) Tauc plots of the diffuse reflectance data: extrapolation of the data to $(F(R)h\nu)^2 = 0$ (indicated by the dashed line) yields the band gap for each material.

susceptibility at low temperatures ($T < 15$ K for $M = \text{Fe}, \text{Co}, \text{Ni}$ and $T < 35$ K for $M = \text{Mn}$), due to small amounts (< 1 wt.%) of paramagnetic impurities and defects, as observed in several other magnetic molecular frameworks.^{9,20,51}

For each compound, the high-temperature ($T > 150$ K) data were fitted to the Curie-Weiss law, yielding values of the Weiss constant, θ , and Curie constant, C [Table 2]. The data collected for $\text{Ni}(\text{NCS})_2$ and $\text{Co}(\text{NCS})_2$ are broadly consistent with previously reported measurements.^{19,27}

The large deviations in $\mu_{\text{eff.}}$ from the spin-only values for $\text{Fe}(\text{NCS})_2$ and $\text{Co}(\text{NCS})_2$ likely arise from spin-orbit coupling, due to the residual orbital angular momentum in the $^5T_{2g}$ and $^4T_{1g}$

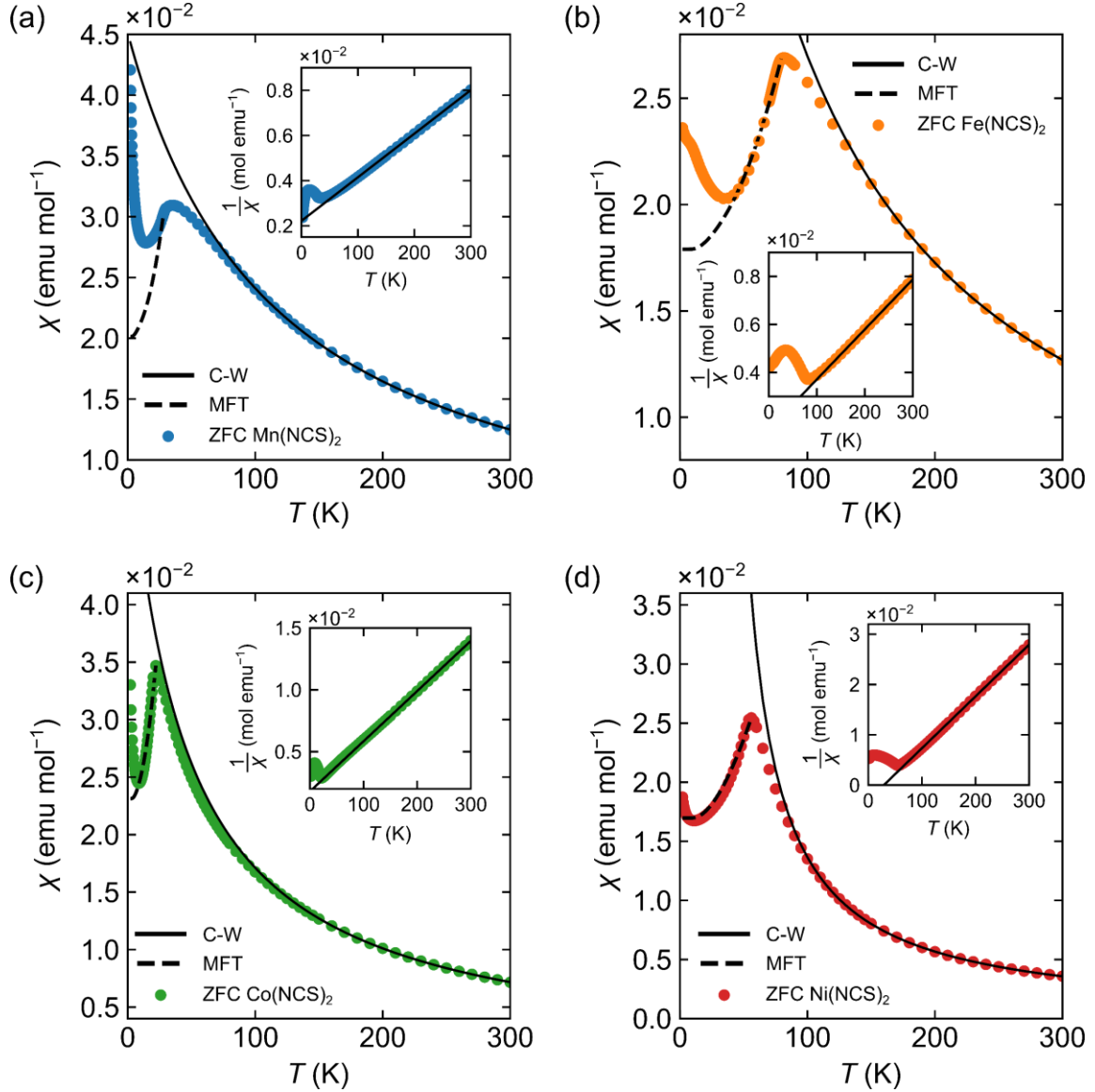


Figure 6. Zero-field cooled (ZFC) magnetic susceptibility data collected for $\text{Mn}(\text{NCS})_2$ (a), $\text{Fe}(\text{NCS})_2$ (b), $\text{Co}(\text{NCS})_2$ (c) and $\text{Ni}(\text{NCS})_2$ (d) in a constant magnetic field strength $H = 0.01$ T. The Curie-Weiss law was used to model the high-temperature ($T > 150$ K) data, while a low-temperature mean-field theory (MFT) model was used for the data $T < T_N$. Insets show the inverse of magnetic susceptibility, used to examine the Curie-Weiss law fit.

terms for high-spin octahedral Fe^{2+} and Co^{2+} , respectively.^{52–55} The observed deviations for $\text{Mn}(\text{NCS})_2$ and $\text{Ni}(\text{NCS})_2$ are much smaller, as no first-order orbital contribution is expected.^{56,57}

We note that net magnetic interactions, as measured by θ , become increasingly antiferromagnetic on moving to earlier TM ions [Figure 7], likely due to the more diffuse nature of M^{2+} 3d orbitals earlier in the series, enabling better spatial overlap with the $(\text{NCS})^-$ σ and π frontier orbitals. The trend in Weiss constants also highlights the considerable increase in the net magnetic interaction strength between

spins on moving to earlier TM ions, particularly for $\text{Mn}(\text{NCS})_2$ and $\text{Fe}(\text{NCS})_2$.

As $M(\text{NCS})_2$ are layered materials with weak van der Waals interactions between the layers, we anticipated these materials would display low-dimensional magnetic behaviour. The ratio $f = |\theta|/T_N$ was computed for each compound, as this parameter may be used to assess the extent to which long-range order is suppressed by low-dimensionality or spin frustration.¹⁵ For $\text{Mn}(\text{NCS})_2$, $f = 4.1(1)$; for $\text{Fe}(\text{NCS})_2$, $f = 0.99(4)$; for $\text{Co}(\text{NCS})_2$, $f = 2.2(1)$ and for $\text{Ni}(\text{NCS})_2$, $f = 0.54(3)$, which do not suggest strong suppression of long-range order.¹⁵

Table 2. Bulk magnetic susceptibility parameters, extracted from the raw magnetic susceptibility data (T_N), high-temperature Curie-Weiss law fits (θ , μ_{eff} and g) and Rietveld refinements of the low-temperature PND data (staggered moments, $m_{\text{sta.}}$). Experimental standard errors are given in parentheses.

	Mn(NCS) ₂	Fe(NCS) ₂	Co(NCS) ₂	Ni(NCS) ₂
θ (K)	-115(3)	-78(3)	-44(1)	+29(1)
T_N (K)	28.0(3)	78.4(3)	20.0(5)	54(2)
$\mu_{\text{eff.}}$ (μ_B)	6.44(5)	6.19(6)	4.44(4)	2.79(2)
g	2.18(2)	2.53(2)	2.29(2)	1.97(1)
$m_{\text{sta.}}$ (μ_B)	4.02(4)	4.82(6)	3.02(2)	1.75(5)

The observed variation in susceptibility below T_N was modelled using a powder-average mean-field theory (MFT) model with Heisenberg exchange [Figure 6].^{58,59} This model qualitatively accounted for the observed magnetic susceptibilities, but could not be used to extract the three nearest neighbour exchange interaction strengths, J_1 , J_2 and J_3 [Figure 2(b)], as these parameters are correlated. We then attempted to determine the values of J_1 , J_2 and J_3 using a reaction-field model.⁶⁰ However, this proved unsuccessful, as strong correlations between the parameters again precluded their reliable determination.

To assess whether any field-induced magnetic phase transitions occur in any of the compounds, isothermal magnetisation measurements ($M(H)$ curves) were carried out [Figures S3–S6]. The $M(H)$ curves show that, in the region -7 to $+7$ T, saturation is not achieved, and that each material undergoes a spin reorientation transition (at $H = \pm 0.35$ T, ± 1.00 T, ± 1.20 and ± 1.35 T for $M = \text{Mn}$, Fe , Co and Ni , respectively).

3.3. Magnetic ground state from neutron diffraction experiments The dominant interactions in the $M(\text{NCS})_2$ frameworks may be understood by examining their ordered magnetic structures. As such, we carried out low-temperature neutron diffraction experiments to determine the magnetic ground state of these frameworks. All four compounds were observed to adopt ordered commensurate ground states.

On cooling $\text{Mn}(\text{NCS})_2$ below T_N ($= 28$ K), superlattice reflections were observed, corresponding to a propagation vector $\mathbf{k} = [100]^*$. Similarly, for $\text{Fe}(\text{NCS})_2$ and $\text{Co}(\text{NCS})_2$, superlattice reflections corresponding to the $\mathbf{k} = [100]^*$ propagation vector were observed

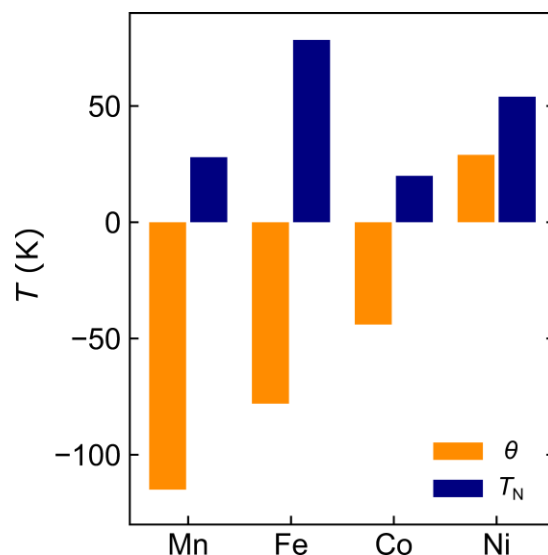


Figure 7. Variation of the Weiss temperature, θ , and Néel temperature, T_N , across the first-row transition metals, M , in the $M(\text{NCS})_2$ family.

below $T_N = 80$ K and 22 K, respectively [Figures 8(a), 8(c), 8(e), S7, S8 and S9]; the temperature dependence of these peaks' intensities are shown in Figures 8(b), (d) and (f). This propagation vector corresponds to breaking of the lattice C -centring, leading to a primitive magnetic cell which is twice the size of the primitive nuclear cell.

Symmetry-mode analysis was used to determine the symmetry-allowed magnetic irreducible representations (irreps), yielding mY_1^+ and mY_2^+ irreps, in Miller and Love's notation,⁶¹ for $\text{Mn}(\text{NCS})_2$, $\text{Fe}(\text{NCS})_2$ and $\text{Co}(\text{NCS})_2$. Rietveld refinement of the data using these irreps revealed that only the mY_2^+ irrep was consistent with the data for $\text{Mn}(\text{NCS})_2$, $\text{Fe}(\text{NCS})_2$ and $\text{Co}(\text{NCS})_2$. The refinements against the mY_2^+ symmetry-adapted mode yielded staggered magnetic moments of $4.02(4) \mu_B$ ($\text{Mn}(\text{NCS})_2$), $4.82(6) \mu_B$ ($\text{Fe}(\text{NCS})_2$) and $3.018(16) \mu_B$ ($\text{Co}(\text{NCS})_2$), with magnetic space group $\text{Pa}2_1/c$ in the BNS notation.⁶²

In contrast to the other members of the $M(\text{NCS})_2$ family, the magnetic Bragg peaks observed below $T_N = 56$ K for $\text{Ni}(\text{NCS})_2$ were indexed to a propagation vector of $\mathbf{k} = \left[00\frac{1}{2}\right]^*$, corresponding to mA_1^+ and mA_2^+ irreps. The neutron diffraction data were consistent with the mA_2^+ -distorted structure and Rietveld refinement against this structure [Figures 8(g) and S10] yielded a staggered moment of $1.73(5) \mu_B$ and a magnetic space group $\text{Cc}2/c$ in

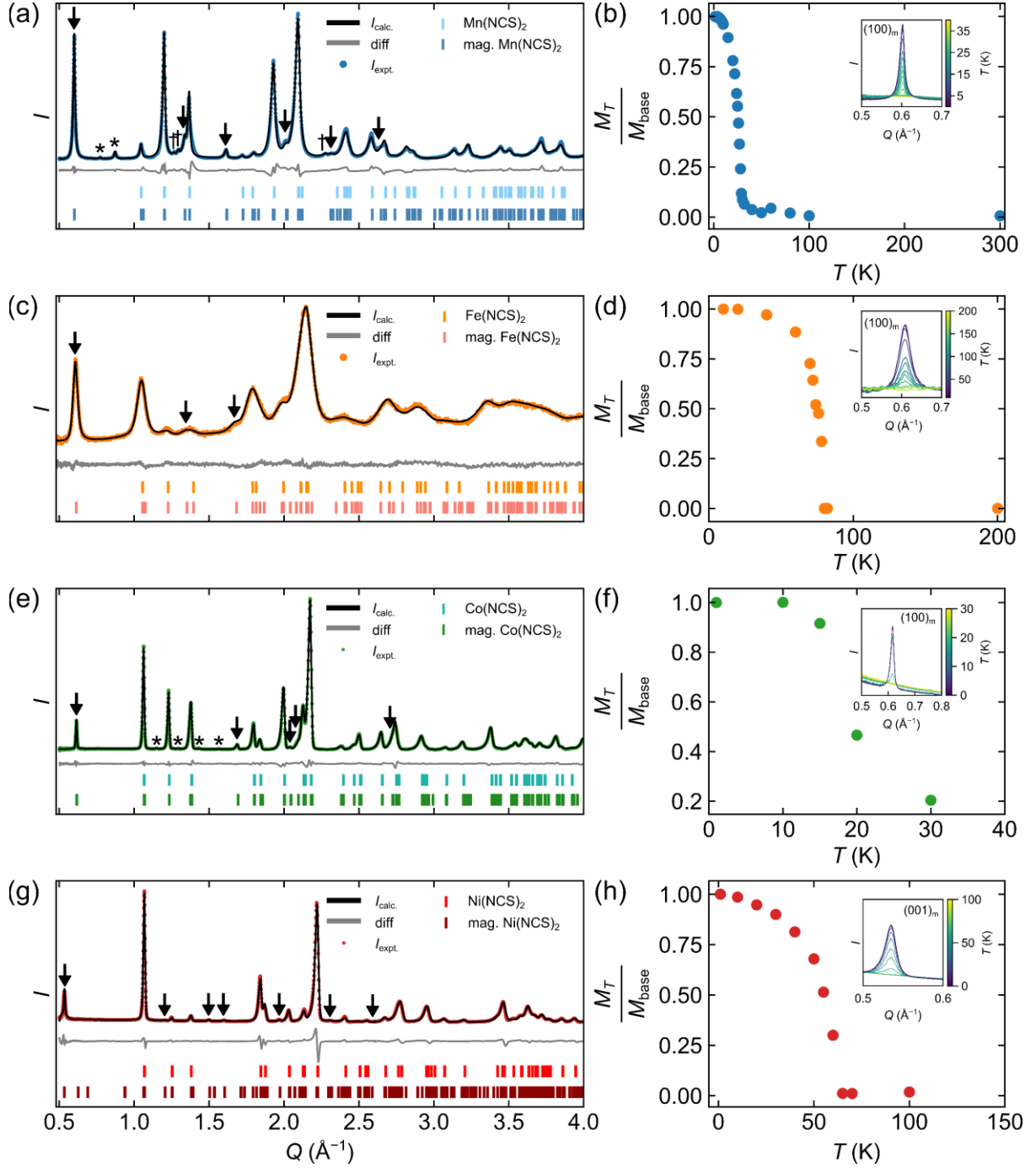


Figure 8. Rietveld fits to the PND patterns between $Q = 0.48 \text{ \AA}^{-1}$ and $Q = 4.00 \text{ \AA}^{-1}$ collected at 1.5 K for Mn(NCS)₂ (a); at 1.5 K for Co(NCS)₂ (e); and at 1.5 K for Ni(NCS)₂ (g), all on Bank 2 of WISH. (c) shows the PND pattern for Fe(NCS)₂ collected at 10 K on Bank 2 of GEM. Arrows lie directly above magnetic reflections from magnetically ordered M(NCS)₂; asterisks are directly above reflections from magnetic impurities, whilst daggers are directly above reflections from non-magnetic impurities. $R_{\text{wp}} = 7.539\%$ for Mn(NCS)₂, 3.303% for Fe(NCS)₂, 4.061% for Co(NCS)₂ and 6.253% for Ni(NCS)₂. (b), (d), (f) and (h) show how the reduced staggered moment (M_T/M_{base} , where M_T is the moment at temperature T and M_{base} the base temperature moment; all moments were obtained from the Rietveld fits) varies as a function of temperature for Mn(NCS)₂, Fe(NCS)₂, Co(NCS)₂ and Ni(NCS)₂, respectively. Insets show how the intensities of the magnetic (100) peaks for Mn(NCS)₂, Fe(NCS)₂ and Co(NCS)₂ and the magnetic (001) peak for Ni(NCS)₂ vary as a function of temperature.

the BNS notation, with the magnetic unit cell doubled along the c -direction, relative to the nuclear cell [Figure 9].

Since Ni(NCS)₂ is ferromagnetic within the layer, we anticipate $J_1/J_2 > -0.5$ and $J_2 < 0$ (i.e. ferromagnetic), so that Ni(NCS)₂ lies in the FM

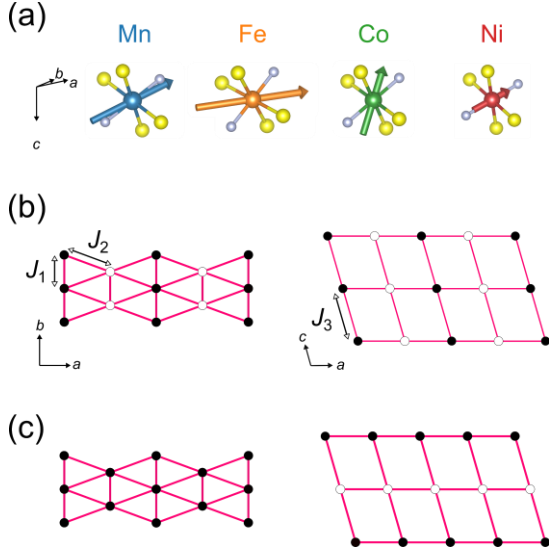


Figure 9. (a) Schematic of the ordered magnetic moments of Mn^{2+} , Fe^{2+} , Co^{2+} and Ni^{2+} in $M(\text{NCS})_2$ (N atoms in grey-blue, S in yellow). The magnetic lattice adopted by $\text{Mn}(\text{NCS})_2$, $\text{Fe}(\text{NCS})_2$ and $\text{Co}(\text{NCS})_2$ is shown in (b), whilst (c) shows the magnetic lattice of $\text{Ni}(\text{NCS})_2$. Filled and empty circles denote collinear moments with opposite spatial orientations.

region of the classical phase diagram [Figure 2(a)]. Likewise, we anticipate $J_1/J_2 < 0.5$ and $J_2 > 0$ for $\text{Mn}(\text{NCS})_2$, $\text{Fe}(\text{NCS})_2$ and $\text{Co}(\text{NCS})_2$, so that these materials occupy the AF region of the classical phase diagram [Figure 2(a)]. Additional constraints on the relative sizes and signs of J_1 and J_2 are established in the Discussion.

The staggered moments of $\text{Fe}(\text{NCS})_2$, $\text{Co}(\text{NCS})_2$ and $\text{Ni}(\text{NCS})_2$ are broadly consistent with the effective magnetic moments measured *via* bulk magnetic susceptibility measurements [Table 2], with deviations from the spin-only values likely arising from delocalisation (covalency) effects (see Discussion).

We also established the temperature dependence of the lattice parameters [Figure S11]. For all members of the $M(\text{NCS})_2$ family, the lattice parameters were observed to vary broadly linearly with temperature, with no discontinuities observed. For $\text{Mn}(\text{NCS})_2$, $\text{Co}(\text{NCS})_2$ and $\text{Ni}(\text{NCS})_2$, the *c*-axis expands most as temperature rises [Figure S11], since the interactions along the *c* axis are primarily weaker van der Waals interactions between the layers. The temperature dependence of lattice parameters for $\text{Fe}(\text{NCS})_2$ could not be accurately determined, due to the breadth of the Bragg peaks.

4. DISCUSSION

The divalent first-row TM thiocyanates $M(\text{NCS})_2$ ($M = \text{Mn}, \text{Fe}, \text{Co}$ and Ni) adopt the same layered crystal structure, with space group $C2/m$. As M changes, we observe broadly linear variations in the lattice parameters with the ionic radius of M^{2+} .

As earlier first-row TM ions occupy the M^{2+} sites in the $M(\text{NCS})_2$ structure, θ becomes increasingly antiferromagnetic [Figure 7], due to (individually) stronger antiferromagnetic interactions and/or weaker ferromagnetic interactions. We expect that the magnetic properties of the $M(\text{NCS})_2$ lattices are dominated by the two nearest neighbour superexchange interactions, J_1 and J_2 , as the interlayer interaction, J_3 , is likely weak, due to the large separation and lack of chemical bonds between M^{2+} ions. The dipolar interactions between M^{2+} are expected to be small, due to the large distances between M^{2+} centres (at least 3.6 Å, corresponding to a dipolar interaction strength on the order of 0.01 K); likewise, we expect direct exchange to be weak, due to the large $M^{2+}-M^{2+}$ distances. Therefore, we expect the strengths of the dominant exchange interactions in $M(\text{NCS})_2$ to depend primarily on the occupation of the magnetic 3*d* orbitals and their overlap with the frontier orbitals on $(\text{NCS})^-$.

The J_1 interaction will likely contain two contributions: firstly, antiferromagnetic superexchange involving overlap between t_{2g} and e_g orbitals on adjacent M^{2+} ions (mediated by a S *p*-like orbital, Figure 10(a)) and secondly, ferromagnetic exchange-correlation-driven superexchange mediated by the two orthogonal sulphur *p*-like orbitals [Figure 10(c)].^{63–65} The antiferromagnetic component will weaken from left to right across the TM series, as the number of unpaired electrons in t_{2g} orbitals decreases, until for $M = \text{Ni}$, the t_{2g} orbitals are fully occupied and we anticipate a negligible antiferromagnetic component. Each metal has the same e_g orbital occupation (e_g^2) and so we expect the ferromagnetic contribution [Figure 10(c)] to be broadly similar in magnitude across the series. Consequently, we expect the J_1 interaction to become increasingly ferromagnetic (more negative J_1) for later TM.

The J_2 superexchange interaction is principally mediated *via* the σ - and π -like frontier orbitals on $(\text{NCS})^-$, dominated by lobes on S and N

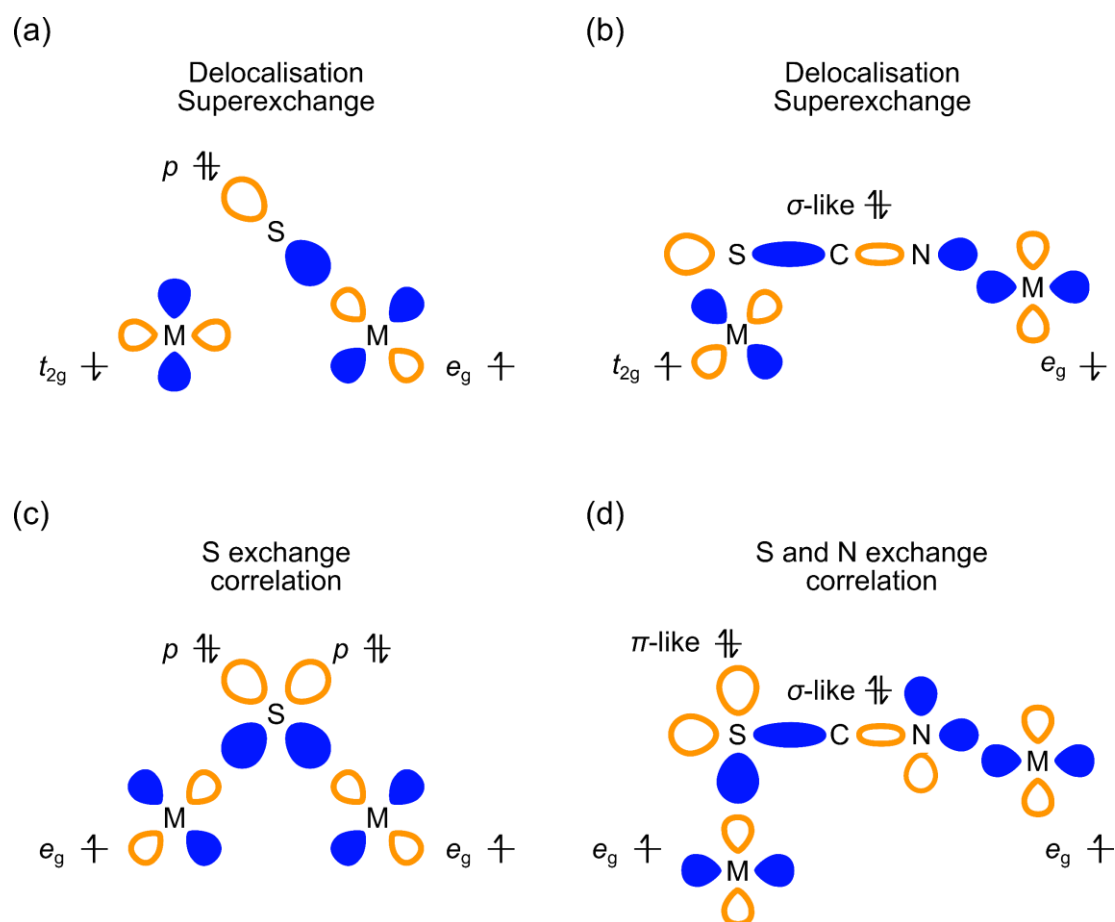


Figure 10. Schematic figures illustrating simplified superexchange mechanisms for the J_1 ((a) and (c)) and J_2 ((b) and (d)) interactions in terms of the magnetic M^{2+} 3d orbitals and frontier σ -like and π -like orbitals on $(\text{NCS})^-$. Orange and blue lobes indicate opposite phases of orbital wavefunctions. The antiferromagnetic components of the J_1 ((a)) and J_2 ((b)) interactions proceed via delocalisation superexchange, whilst the ferromagnetic components proceed via exchange correlation—either via S only for J_1 ((c)) or via S and N for J_2 ((d)).

atoms [Figure 10 (b) and (d)].⁹ An antiferromagnetic contribution will arise from delocalisation superexchange between metal t_{2g} and e_g orbitals via the σ -like frontier orbital on $(\text{NCS})^-$ [Figure 10(b)]. A countervailing ferromagnetic interaction will be produced by exchange correlation between the metal e_g orbitals on M^{2+} , mediated by the orthogonal σ - and π -like frontier orbitals on $(\text{NCS})^-$ [Figure 10(d)]. Again, as electrons are added to the t_{2g} orbitals (from Mn^{2+} to Ni^{2+}), the antiferromagnetic component of the J_2 interaction will weaken and become negligible for $M = \text{Ni}$, resulting in a more ferromagnetic J_2 . Indeed, for many $M(\text{NCS})_2$ solvate frameworks (those of the form $M(\text{NCS})_2L_x$, where L = ligand), the Ni member of the family orders ferromagnetically along the Ni–NCS–Ni chains, whilst the Mn and Co members order antiferromagnetically,^{22,24,51,66,67} consistent with our experimental results and proposed magnetochemical mechanisms.

Deviations from the ‘ideal’ 90° M –S– M and 180° M –(NCS)– M bond angles will likely mix the ferromagnetic and antiferromagnetic components of each interaction, giving deviations from the trends we explain above. Nevertheless, our qualitative predictions of the signs and strengths of the J_1 and J_2 interactions are borne out by the observed magnetic ground states and trends in the bulk magnetic properties.

We anticipate that these materials will show similar magnetic behaviour to two-dimensional systems, despite ordering as bulk antiferromagnets, as we expect the interlayer interactions (J_3) to be weak. Therefore, our magnetochemical model allows us to rationalise the location of each compound in the classical two-dimensional magnetic phase diagram [Figure 2(a)]. For $M = \text{Mn}$, Fe and Co, we expect $J_2 > 0$ (i.e. antiferromagnetic), whilst we expect J_1 to be small and either

ferromagnetic or antiferromagnetic, due to cancellation of the superexchange contributions. This predicts that these materials all lie in the AF region of the phase diagram, as observed from their ground state magnetic structures. As J_1 becomes more antiferromagnetic, we anticipate moderate geometric frustration with the antiferromagnetic J_2 , and indeed f is largest for $\text{Mn}(\text{NCS})_2$. For $M = \text{Ni}$, we anticipate J_1 and J_2 to be ferromagnetic (i.e. $J_1, J_2 < 0$), placing it in the FM region of the phase diagram, as observed.

For all members of the $M(\text{NCS})_2$ family, the size of the staggered moments obtained from PND are all lower than the size of the expected maximum ordered moment (i.e. gS). This likely corresponds to a covalency effect, where spin density is transferred from M^{2+} to the $(\text{NCS})^-$ ligand.⁶⁸

Finally, we find that the ordered moment lies broadly along the N–M–N axis for $\text{Mn}(\text{NCS})_2$ and $\text{Ni}(\text{NCS})_2$, suggesting significant spin density in the d orbital pointing along that axis. For $\text{Fe}(\text{NCS})_2$ and $\text{Co}(\text{NCS})_2$, the moment has a significant tilt away from the N–M–N axis, towards the meridional plane containing S-bound $(\text{NCS})^-$ ligands, suggesting the important role of spin-orbit effects. Future electron spin resonance spectroscopy investigations will shed further light on the origin of these differences.

Recent work on CrI_3 and $\text{Cr}_2\text{Ge}_2\text{Te}_6$ has shown that mechanical exfoliation of layered ferromagnets can generate single-layer magnets.^{69–71} While bulk $\text{Ni}(\text{NCS})_2$ orders as a three-dimensional antiferromagnet, the combination of ferromagnetic intralayer order with weak interlayer interactions suggests that monolayers of this may host single-layer ferromagnetism, provided there is sufficient anisotropy. These single-layer ferromagnets may have applications as magnetoelectronic devices, ferromagnetic light emitters^{69,70} and hybrid multilayer materials,^{72,73} motivating future synthetic studies.

5. CONCLUSION

In this work, we have determined how the strengths of magnetic interactions vary across the first-row TM pseudobinary thiocyanates, $M(\text{NCS})_2$. Two new materials— $\text{Mn}(\text{NCS})_2$ and $\text{Fe}(\text{NCS})_2$ —are reported, alongside the

magnetic structures of these materials and of $\text{Co}(\text{NCS})_2$ and $\text{Ni}(\text{NCS})_2$. Based on the observed magnetic structures, we have qualitatively rationalised the relative strengths and signs of the nearest-neighbour in-plane exchange interactions, J_1 and J_2 , and have located each material on the magnetic phase diagram of the spatially anisotropic triangular lattice.

On moving to TM ions earlier in the row, the net magnetic interactions become stronger and increasingly antiferromagnetic, with the Weiss constant reaching $-115(3)$ K for $\text{Mn}(\text{NCS})_2$ and the Néel temperature of $\text{Fe}(\text{NCS})_2$ reaching above 78 K.

PND revealed that $\text{Mn}(\text{NCS})_2$, $\text{Fe}(\text{NCS})_2$ and $\text{Co}(\text{NCS})_2$ adopt the same commensurate antiferromagnetic structure, in which parallel spins along the crystallographic b axis order antiferromagnetically along the a axis; these layers of spins are then stacked antiferromagnetically along the c -direction. In contrast, the magnetic structure of $\text{Ni}(\text{NCS})_2$ comprises ferromagnetically ordered ab layers ordered antiferromagnetically along the c -axis. This suggests that single-layer $\text{Ni}(\text{NCS})_2$ may be a candidate monolayer ferromagnet belonging to a new family of magnetic frameworks. The results collected from this study open up new avenues for the rational design of magnetic molecular framework materials.

AUTHOR INFORMATION

Corresponding Authors

*E-mail: cpg27@cam.ac.uk;
matthew.cliffe@nottingham.ac.uk

ORCID

Euan N. Bassey: 0000-0001-8827-7175
 Joseph A.M. Paddison: 0000-0002-2274-0988
 Evan N. Keyzer: 0000-0002-0655-2813
 Jeongjae Lee: 0000-0003-4294-4993
 Pascal Manuel: 0000-0002-8845-6576
 Ivan da Silva: 0000-0002-4472-9675
 Siân E. Dutton: 0000-0003-0984-5504
 Clare P. Grey: 0000-0001-5572-192X
 Matthew J. Cliffe: 0000-0002-0408-7647

Notes

There are no conflicts of interest to declare.

ACKNOWLEDGEMENTS

E.N.B. thanks the EPSRC for financial support. J.A.M.P.'s work at Cambridge was supported by Churchill College, University of Cambridge. J.A.M.P.'s work at ORNL was supported by ORNL LDRD 10004 (discussion of magnetic modelling) and the U.S. Department of Energy, Office of Science, Basic Energy Sciences, Materials Sciences and Engineering Division (computational resources). E.N.K. thanks NSERC of Canada for a PGSD. J.L. thanks Trinity College, University of Cambridge for financial support. M.J.C. acknowledges the School of Chemistry, University of Nottingham for a Hobday Fellowship. Magnetic measurements were carried out using the Advanced Materials Characterisation Suite, funded by EPSRC Strategic Equipment Grant EP/M000524/1. We also acknowledge the Rutherford Appleton Laboratory for access to the ISIS Neutron Source.

REFERENCES

- (1) Ramesh, R. Emerging Routes to Multiferroics. *Nature* **2009**, *461* (7268), 1218–1219.
- (2) Stroppa, A.; Barone, P.; Jain, P.; Perez-Mato, J. M.; Picozzi, S. Hybrid Improper Ferroelectricity in a Multiferroic and Magnetoelectric Metal-Organic Framework. *Adv. Mater.* **2013**, *25* (16), 2284–2290.
- (3) Boström, H. L. B.; Senn, M. S.; Goodwin, A. L. Recipes for Improper Ferroelectricity in Molecular Perovskites. *Nat. Commun.* **2018**, *9* (1), 2380.
- (4) Wang, Z.; Jain, P.; Choi, K.-Y.; Van Tol, J.; Cheetham, A. K.; Kroto, H. W.; Koo, H.-J.; Zhou, H.; Hwang, J.; Choi, E. S.; Whangbo, M.-H.; Dalal, N. S. Dimethylammonium Copper Formate [(CH₃)₂NH₂]₂Cu(HCOO)₃: A Metal-Organic Framework with Quasi-One-Dimensional Antiferromagnetism and Magnetoelectricity. *Phys. Rev. B* **2013**, *87* (22), 224406-1-224406-224408.
- (5) Maspoch, D.; Ruiz-Molina, D.; Veciana, J. Magnetic Nanoporous Coordination Polymers. *J. Mater. Chem.* **2004**, *14* (18), 2713–2723.
- (6) Motokawa, N.; Matsunaga, S.; Takaishi, S.; Miyasaka, H.; Yamashita, M.; Dunbar, K. R. Reversible Magnetism between an Antiferromagnet and a Ferromagnet Related to Solvation/Desolvation in a Robust Layered [Ru₂]2TCNQ Charge-Transfer System. *J. Am. Chem. Soc.* **2010**, *132*, 11943–11951.
- (7) Maspoch, D.; Ruiz-Molina, D.; Wurst, K.; Domingo, N.; Cavallini, M.; Biscarini, F.; Tejada, J.; Rovira, C.; Veciana, J. A Nanoporous Molecular Magnet with Reversible Solvent-Induced Mechanical and Magnetic Properties. *Nat. Mater.* **2003**, *2* (3), 190–195.
- (8) Cairns, A. B.; Goodwin, A. L. Structural Disorder in Molecular Framework Materials. *Chem. Soc. Rev.* **2013**, *42* (12), 4881.
- (9) Cliffe, M. J.; Lee, J.; Paddison, J. A. M.; Schott, S.; Mukherjee, P.; Gaultois, M. W.; Manuel, P.; Sirringhaus, H.; Dutton, S. E.; Grey, C. P. Low-Dimensional Quantum Magnetism in Cu(NCS)₂, a Molecular Framework Material. *Phys. Rev. B* **2017**, *97* (14), 144421.
- (10) Greenfield, J. T.; Kamali, S.; Izquierdo, N.; Chen, M.; Kovnir, K. NH₄FeCl₂(HCOO): Synthesis, Structure, and Magnetism of a Novel Low-Dimensional Magnetic Material. *Inorg. Chem.* **2014**, *53* (6), 3162–3169.
- (11) Saines, P. J.; Paddison, J. A. M.; Thygesen, P. M. M.; Tucker, M. G. Searching beyond Gd for Magnetocaloric Frameworks: Magnetic Properties and Interactions of the Ln(HCOO)₃ Series. *Mater. Horizons* **2015**, *2* (5), 528–535.
- (12) Kurmoo, M.; Kepert, C. J. Hard Magnets Based on Transition Metal Complexes with the Dicyanamide Anion, [N(CN)₂]⁻. *New J. Chem.* **1998**, *22*, 1515–1524.
- (13) Saines, P. J.; Bristowe, N. C. Probing Magnetic Interactions in Metal-Organic Frameworks and Coordination Polymers Microscopically. *Dalton Transactions*. Royal Society of Chemistry 2018, pp 13257–13280.
- (14) Böhme, M.; Jochim, A.; Rams, M.; Lohmiller, T.; Suckert, S.; Schnegg, A.; Plass, W.; Näther, C. Variation of the Chain Geometry in Isomeric 1D Co(NCS)₂ Coordination Polymers and Their Influence on the Magnetic Properties. *Inorg. Chem.* **2020**, *59* (8), 5325–5338.
- (15) Landee, C. P.; Turnbull, M. M. Review: A Gentle Introduction to Magnetism: Units, Fields, Theory, and Experiment. *J. Coord. Chem.* **2014**, *67* (3), 375–439.
- (16) Balents, L. Spin Liquids in Frustrated Magnets. *Nature* **2010**, *464* (7286), 199–208.
- (17) Wen, J.; Yu, S.-L.; Li, S.; Yu, W.; Li, J.-X. Experimental Identification of Quantum Spin Liquids. *npj Quantum Mater.* **2019**, *4* (1), 12.
- (18) Lee, P. A.; Nagaosa, N.; Wen, X.-G. Doping a Mott Insulator: Physics of High-Temperature Superconductivity. *Rev. Mod. Phys.* **2006**, *78* (1), 17–85.
- (19) Shurdha, E.; Lapidus, S. H.; Stephens, P. W.; Moore, C. E.; Rheingold, A. L.; Miller, J. S. Extended Network Thiocyanate- and Tetracyanoethanide-Based First-Row Transition Metal Complexes. *Inorg. Chem.* **2012**, *51* (18), 9655–9665.
- (20) Shurdha, E.; Moore, C. E.; Rheingold, A. L.; Lapidus, S. H.; Stephens, P. W.; Arif, A. M.; Miller, J. S. First Row Transition Metal(II) Thiocyanate Complexes, and Formation of 1-, 2-, and 3-Dimensional Extended Network Structures of M(NCS)₂(Solvent)₂ (M = Cr, Mn, Co) Composition. *Inorg. Chem.* **2013**, *52* (18), 10583–10594.
- (21) Reller, A.; Oswald, H. R. Mechanism and Kinetics of Thermal Decompositions of Solids Governed by Phase-Boundary Processes. *J. Solid State*

- Chem.* **1986**, 62 (3), 306–316.
- (22) Boeckmann, J.; Näther, C. Metamagnetism and Long Range Ordering in μ -1,3 Bridging Transition Metal Thiocyanato Coordination Polymers. *Polyhedron* **2012**, 31 (1), 587–595.
- (23) Julve, M.; Verdaguer, M.; De Munno, G.; Real, J. A.; Bruno, G. Synthesis, Crystal Structure, and Magnetic Properties of (μ -Bipyrimidine)(Cyanato)Copper(II) and-(Thiocyanato)Copper(II) Complexes. *Inorg. Chem.* **1993**, 32 (6), 795–802.
- (24) DeFotis, G. C.; Harlan, E. W.; Remy, E. D.; Dell, K. D. Ferromagnetism of $\text{Ni}(\text{SCN})_2(\text{C}_2\text{H}_5\text{OH})_2$. *J. Appl. Phys.* **1991**, 69, 6004–6006.
- (25) Dhers, S.; Feltham, H. L. C.; Brooker, S. A Toolbox of Building Blocks, Linkers and Crystallisation Methods Used to Generate Single-Chain Magnets. *Coord. Chem. Rev.* **2015**, 296, 24–44.
- (26) Dubler, E.; Reller, A.; Oswald, H. R. Intermediates in Thermal Decomposition of Nickel(II) Complexes: The Crystal Structures of $\text{Ni}(\text{SCN})_2(\text{NH}_3)_2$ and $\text{Ni}(\text{SCN})_2$. *Zeitschrift für Krist. - Cryst. Mater.* **1982**, 161 (1–4), 265–278.
- (27) DeFotis, G. C.; Dell, K. D.; Krovich, D. J.; Brubaker, W. W. Antiferromagnetism of $\text{Ni}(\text{SCN})_2$. *J. Appl. Phys.* **1993**, 73 (10), 5386–5388.
- (28) Ramirez, A. P. Strongly Geometrically Frustrated Magnets. *Annu. Rev. Mater. Sci.* **1994**, 24 (1), 453–480.
- (29) Tokunaga, Y.; Okuyama, D.; Kurumaji, T.; Arima, T.; Nakao, H.; Murakami, Y.; Taguchi, Y.; Tokura, Y. Multiferroicity in NiBr_2 with Long-Wavelength Cycloidal Spin Structure on a Triangular Lattice. *Phys. Rev. B* **2011**, 84 (6), 060406.
- (30) Kurumaji, T.; Seki, S.; Ishiwata, S.; Murakawa, H.; Kaneko, Y.; Tokura, Y. Magnetoelectric Responses Induced by Domain Rearrangement and Spin Structural Change in Triangular-Lattice Helimagnets NiI_2 and CoI_2 . *Phys. Rev. B* **2013**, 87 (1), 014429.
- (31) Kurumaji, T.; Seki, S.; Ishiwata, S.; Murakawa, H.; Tokunaga, Y.; Kaneko, Y.; Tokura, Y. Magnetic-Field Induced Competition of Two Multiferroic Orders in a Triangular-Lattice Helimagnet MnI_2 . *Phys. Rev. Lett.* **2011**, 106 (16), 167206.
- (32) Kuindersma, S. R.; Sanchez, J. P.; Haas, C. Magnetic and Structural Investigations on NiI_2 and CoI_2 . *Phys. B+C* **1981**, 111 (2–3), 231–248.
- (33) Bai, X.; Zhang, S.-S.; Dun, Z.; Zhang, H.; Huang, Q.; Zhou, H.; Stone, M. B.; Kolesnikov, A. I.; Ye, F.; Batista, C. D.; Mourigal, M. Hybridized Quadrupolar Excitations in the Spin-Anisotropic Frustrated Magnet FeI_2 . **2020**.
- (34) Schmidt, B.; Thalmeier, P. Neel Temperature and Reentrant H-T Phase Diagram of Quasi-2D Frustrated Magnets. *Phys. Rev. B* **2017**, 96, 214443-1-214443–16.
- (35) Schmidt, B.; Thalmeier, P. Quantum Fluctuations in Anisotropic Triangular Lattices with Ferromagnetic and Antiferromagnetic Exchange. *Phys. Rev. B* **2014**, 89 (18), 184402-1-184402–184412.
- (36) Nakayama, G.; Hara, S.; Sato, H.; Narumi, Y.; Nojiri, H. Synthesis and Magnetic Properties of a New Series of Triangular-Lattice Magnets, $\text{Na}_2\text{BaMV}_2\text{O}_8$ ($M = \text{Ni}, \text{Co}, \text{and Mn}$). *J. Phys. Condens. Matter* **2013**, 25 (11).
- (37) Pawley, G. S. Unit-Cell Refinement from Powder Diffraction Scans. *J. Appl. Crystallogr.* **1981**, 14 (6), 357–361.
- (38) Rietveld, H. M. Line Profiles of Neutron Powder-Diffraction Peaks for Structure Refinement. *Acta Crystallogr.* **1967**, 22 (1), 151–152.
- (39) Rietveld, H. M. A Profile Refinement Method for Nuclear and Magnetic Structures. *J. Appl. Crystallogr.* **1969**, 2 (2), 65–71.
- (40) Coelho, A. A. TOPAS and TOPAS-Academic: An Optimization Program Integrating Computer Algebra and Crystallographic Objects Written in C++. *J. Appl. Crystallogr.* **2018**, 51 (1), 210–218.
- (41) Coelho, A. TOPAS-Academic: General Profile and Structure Analysis Software for Powder Diffraction Data. Brisbane, Australia 2007.
- (42) Bain, G. A.; Berry, J. F. Diamagnetic Corrections and Pascal's Constants. *J. Chem. Educ.* **2008**, 85 (4), 532–536.
- (43) Chapon, L. C.; Manuel, P.; Radaelli, P. G.; Benson, C.; Perrott, L.; Ansell, S.; Rhodes, N. J.; Raspino, D.; Duxbury, D.; Spill, E.; Norris, J. Wish: The New Powder and Single Crystal Magnetic Diffractometer on the Second Target Station. *Neutron News* **2011**, 22 (2), 22–25.
- (44) Arnold, O.; Bilheux, J. C.; Borreguero, J. M.; Buts, A.; Campbell, S. I.; Chapon, L.; Doucet, M.; Draper, N.; Ferraz Leal, R.; Gigg, M. A.; Lynch, V. E.; Markvardsen, A.; Mikkelsen, D. J.; Mikkelsen, R. L.; Miller, R.; Palmen, K.; Parker, P.; Passos, G.; Perring, T. G.; Peterson, P. F.; Ren, S.; Reuter, M. A.; Savici, A. T.; Taylor, J. W.; Taylor, R. J.; Tolchenov, R.; Zhou, W.; Zikovsky, J. Mantid—Data Analysis and Visualization Package for Neutron Scattering and μ SR Experiments. *Nucl. Instruments Methods Phys. Res. Sect. A Accel. Spectrometers, Detect. Assoc. Equip.* **2014**, 764, 156–166.
- (45) Shannon, R. D. Revised Effective Ionic Radii and Systematic Studies of Interatomic Distances in Halides and Chalcogenides. *Acta Crystallogr. Sect. A* **1976**, 32 (5), 751–767.
- (46) Cliffe, M. J.; Keyzer, E. N.; Dunstan, M. T.; Ahmad, S.; De Volder, M. F. L.; Deschler, F.; Morris, A. J.; Grey, C. P. Strongly Coloured Thiocyanate Frameworks with Perovskite-Analogue Structures. *Chem. Sci.* **2019**, 10 (3), 793–801.
- (47) Addison, A. W.; Butcher, R. J.; Homonnay, Z.; Pavlishchuk, V. V.; Prushan, M. J.; Thompson, L. K. The Hexakis(Thiocyanato)Ferrate(III) Ion: A Coordination Chemistry Classic Reveals an Interesting Geometry Pattern for the Thiocyanate Ligands. *Eur. J. Inorg. Chem.* **2005**, 2005 (12), 2404–2408.
- (48) Dinsdale, D. R.; Lough, A. J.; Lemaire, M. T. Structure and Magnetic Properties of an Unusual

- Homoleptic Iron(III) Thiocyanate Dimer. *Dalt. Trans.* **2015**, 44 (24), 11077–11082.
- (49) Rosseinsky, D. R.; Dorrity, I. A. Ligand Field Parameters and Spectra of First-Row Transition Metal Dihalides in the Solid State. *Coord. Chem. Rev.* **1978**, 25 (1), 31–67.
- (50) Tauc, J. Optical Properties and Electronic Structure of Amorphous Ge and Si. *Mater. Res. Bull.* **1968**, 3 (1), 37–46.
- (51) Wöhlert, S.; Fink, L.; Schmidt, M. U.; Näther, C. Synthesis and Characterization of New 2D Coordination Polymers Based on Mn(NCS)₂ and Ni(NCS)₂ with 1, 2-Bis(4-Pyridyl)-Ethane as Co-Ligand. *Zeitschrift für Anorg. und Allg. Chemie* **2013**, 639 (12–13), 2186–2194.
- (52) Tanabe, Y.; Sugano, S. On the Absorption Spectra of Complex Ions. *J. Phys. Soc. Japan* **1954**, 9 (5), 753–766.
- (53) Tanabe, Y.; Sugano, S. On the Absorption Spectra of Complex Ions II. *J. Phys. Soc. Japan* **1954**, 9 (5), 766–779.
- (54) Tanabe, Y.; Sugano, S. On the Absorption Spectra of Complex Ions, III The Calculation of the Crystalline Field Strength. *J. Phys. Soc. Japan* **1956**, 11 (8), 864–877.
- (55) Figgis, B. N.; Lewis, J. *The Magnetic Properties of Polynuclear Transition Metal Complexes*; 1964; Vol. 6.
- (56) Lovesey, S. W. Magnetic Excitations in FeCl₂. *J. Phys. C Solid State Phys.* **1974**, 7 (11), 2049–2059.
- (57) Hutchings, M. T. Neutron Scattering Investigation of Magnetic Excitations in CoCl₂. *J. Phys. C Solid State Phys.* **1973**, 6 (21), 3143–3155.
- (58) Johnston, D. C. Magnetic Susceptibility of Collinear and Noncollinear Heisenberg Antiferromagnets. *Phys. Rev. Lett.* **2012**, 109 (7), 077201-1-077201–077205.
- (59) Johnston, D. C. Unified Molecular Field Theory for Collinear and Noncollinear Heisenberg Antiferromagnets. *Phys. Rev. B* **2015**, 91 (6), 064427-1-064427–27.
- (60) Onsager, L. Crystal Statistics. I. A Two-Dimensional Model with an Order-Disorder Transition. *Phys. Rev.* **1944**, 65 (3–4), 117–149.
- (61) Cracknell, A. P.; Davies, B. L.; Miller, S. C.; Love, W. F. *Kronecker Product Tables*; IFI/Plenum: New York, 1979.
- (62) Gallego, S. V.; Tasci, E. S.; de la Flor, G.; Perez-Mato, J. M.; Aroyo, M. I.; IUCr. Magnetic Symmetry in the Bilbao Crystallographic Server: A Computer Program to Provide Systematic Absences of Magnetic Neutron Diffraction. *J. Appl. Crystallogr.* **2012**, 45 (6), 1236–1247.
- (63) Goodenough, J. B. An Interpretation of the Magnetic Properties of the Perovskite-Type Mixed Crystals La(1-x)Sr(x)CoO(3-Y). *J. Phys. Chw. Solids Pergamon Press* **1958**, 6, 287–297.
- (64) Kanamori, J. Theory of the Magnetic Properties of Ferrous and Cobaltous Oxides, I. *Prog. Theor. Phys.* **1957**, 17 (2), 177–196.
- (65) Kanamori, J. Theory of the Magnetic Properties of Ferrous and Cobaltous Oxides, II. *Prog. Theor. Phys.* **1957**, 17 (2), 197–222.
- (66) DeFotis, G. C.; McGhee, E. M.; Echols, K. R.; Wiese, R. S. Magnetic and Structural Properties of Mn(SCN)₂(ROH)₂ Compounds. *J. Appl. Phys.* **1988**, 63 (8), 3569–3571.
- (67) DeFotis, G. C.; Wimberly, B. T.; Jeffers, R. B.; May, W. M.; Owens, T. M. Magnetic Behavior of Single-Crystal Co(SCN)₂(CH₃OH)₂: Three-Dimensional Ising Metamagnetism and Field-Induced Spin Reorientations. *Phys. Rev. B* **2007**, 76 (1), 014419-1-014419–7.
- (68) Kmety, C. R.; Huang, Q.; Lynn, J. W.; Erwin, R. W.; Manson, J. L.; McCall, S.; Crow, J. E.; Stevenson, K. L.; Miller, J. S.; Epstein, A. J. Noncollinear Antiferromagnetic Structure of the Molecule-Based Magnet Mn[N(CN)₂]₂. *Phys. Rev. B* **2000**, 62 (9), 5576–5588.
- (69) Huang, B.; Clark, G.; Navarro-Moratalla, E.; Klein, D. R.; Cheng, R.; Seyler, K. L.; Zhong, D.; Schmidgall, E.; McGuire, M. A.; Cobden, D. H.; Yao, W.; Xiao, D.; Jarillo-Herrero, P.; Xu, X. Layer-Dependent Ferromagnetism in a van Der Waals Crystal down to the Monolayer Limit. *Nature* **2017**, 546 (7657), 270–273.
- (70) Gong, C.; Li, L.; Li, Z.; Ji, H.; Stern, A.; Xia, Y.; Cao, T.; Bao, W.; Wang, C.; Wang, Y.; Qiu, Z. Q.; Cava, R. J.; Louie, S. G.; Xia, J.; Zhang, X. Discovery of Intrinsic Ferromagnetism in Two-Dimensional van Der Waals Crystals. *Nature* **2017**, 546 (7657), 265–269.
- (71) López-Cabrelles, J.; Mañas-Valero, S.; Vitorica-Yrezabal, I. J.; Bereciartua, P. J.; Rodríguez-Velamazán, J. A.; Waerenborgh, J. C.; Vieira, B. J. C.; Davidovikj, D.; Steeneken, P. G.; van der Zant, H. S. J.; Mínguez Espallargas, G.; Coronado, E. Isorecticular Two-Dimensional Magnetic Coordination Polymers Prepared through Pre-Synthetic Ligand Functionalization. *Nat. Chem.* **2018**, 10 (10), 1001–1007.
- (72) Hornick, C.; Rabu, P.; Drillon, M. Hybrid Organic–Inorganic Multilayer Materials: Influence of π Electrons as Magnetic Media in a Series of Bridged-Layer Compounds M₂(OH)(4-x)A(x/2) (M=Cu(II) or Co(II), A=dicarboxylate Anion). *Polyhedron* **2000**, 19 (3), 259–266.
- (73) Rabu, P.; Drillon, M.; Awaga, K.; Fujita, W.; Sekine, T. Hybrid Organic-Inorganic Multilayer Compounds: Towards Controllable and/or Switchable Magnets. In *Magnetism: Molecules to Materials*; Wiley-VCH Verlag GmbH & Co. KGaA: Weinheim, Germany, 2003; pp 357–395.